Breaking of Progressive Internal Gravity Waves: Convective Instability and Shear Instability*

WEI LIU

Center for Climatic Research, and Department of Atmospheric and Oceanic Sciences, University of Wisconsin—Madison, Madison, Wisconsin

FRANCIS P. BRETHERTON

Department of Atmospheric and Oceanic Sciences, University of Wisconsin—Madison, Madison, Wisconsin

ZHENGYU LIU

Center for Climatic Research, and Department of Atmospheric and Oceanic Sciences, University of Wisconsin—Madison, Madison, Wisconsin

LESLIE SMITH

Department of Mathematics and Engineering Physics, University of Wisconsin—Madison, Madison, Wisconsin

HAO LU AND CHRISTOPHER J. RUTLAND

Department of Mechanical Engineering, University of Wisconsin—Madison, Madison, Wisconsin

ABSTRACT

The breaking of a monochromatic two-dimensional internal gravity wave is studied using a newly developed spectral/pseudospectral model. The model features vertical nonperiodic boundary conditions that ensure a realistic simulation of wave breaking during the wave propagation. Isopycnal overturning is induced at a local wave steepness of $s_c = 0.75$–0.79, which is below the conventional threshold of $s = 1$. Isopycnal overturning is a sufficient condition for subsequent wave breaking by convective instability. When $s = s_c$, little primary wave energy is being transferred to high-mode harmonics. Beyond $s = 1$, high-mode harmonics grow rapidly. Primary wave energy is more efficiently transferred by waves of lower frequency. A local gradient Richardson number is defined as $R_i = -(g/\rho_0)(d\rho/dz)/\zeta^2$ to isolate convective instability ($R_i \leq 0$) and wave-induced shear instability ($0 < R_i < 0.25$), where $d\rho/dz$ is the local vertical density gradient and ζ is the horizontal vorticity. Consistent with linear wave theory, the probability density function (PDF) for occurrence of convective instability has a maximum at wave phase $\phi = \pi/2$, where the wave-induced density perturbations to the background stratification are the greatest, whereas the wave-induced shear instability has maxima around $\phi = 0$ (wave trough) and $\phi = \pi$ (wave crest). Nonlinearities in the wave-induced flow broaden the phase span in PDFs of both instabilities. Diapycnal mixing in numerical simulations may be compared with that in realistic oceanic flows in terms of the Cox number. In the numerical simulations, the Cox numbers increase from 1.5 ($s = 0.78$) to 21.5 ($s = 1.1$), and the latter is in the lower range of reported values for the ocean.

Corresponding author address: Wei Liu, Center for Climatic Research, University of Wisconsin—Madison, 1225 W. Dayton St., 1143, Madison, WI 53706.
E-mail: wliu5@wisc.edu

1. Introduction

It has long been believed that vertical mixing in the main thermocline is a dominant factor in governing the intensity of the large-scale thermohaline circulation (Stommel and Webster 1962; Munk 1966). An important source of turbulence and mixing is internal waves that produce significant diapycnal fluxes of momentum and heat (Gregg

1987). Except in some regions with strong baroclinic instability, the breaking of internal waves is a principal contributor to pelagic turbulence and mixing on the vertical scale of a few meters (Munk and Wunsch 1998).

The internal waves can be generated by tidal waves interacting with rough bottom topography. Wave breaking caused by this type of internal waves has received great attention in recent years (e.g., Polzin et al. 1997). In this work, however, we will focus instead on downward-propagating internal waves generated directly or indirectly by the surface wind. Such wind-generated internal waves radiate from near the ocean surface into the deeper main thermocline below and may generate significant background mixing there. They are, however, apparently also reflected by the abyssal waters into upward-propagating waves of comparable wavenumber and amplitude. The model spectrum GM79, which was formulated by Garrett and Munk (1979) to summarize the statistics of observed internal waves throughout the upper ocean, is symmetric between upward and downward pointing wavenumbers and hence also the flux of wave energy.

In general, the breaking of internal waves can be caused by two types of instability (Thorpe 1978, 1979). The first type is shear instability (Kelvin–Helmholtz instability; Miles 1961; Howard 1961), in which disturbances grow in the shear generated by an existing internal wave acting on a sufficiently abrupt vertical transition in density. The second type is convective instability (Orlanski and Bryan 1969; McEwan 1973), which is characterized by the isopycnal steepness reaching and passing beyond the vertical to generate a local density overturning followed by Rayleigh–Taylor instability. Numerous studies have been carried out on these instabilities, including direct numerical simulation (DNS; Bouruet-Aubertot et al. 2001; Koudella and Staquet 2006; Sutherland 2001; Fritts et al. 2003, 2006, 2009a,b). However, a detailed numerical modeling study of the breaking of progressive internal waves has not been published. Indeed, virtually all of previous direct numerical simulations on the internal wave breaking are based on a spectral model with periodic boundary conditions and are driven by a body forcing, which is not suitable for describing the breaking process of progressive internal gravity waves in the oceanic context. First, the momentum and density fields are subject to random changes as waves break; thus, the boundary condition in the direction of wave propagation can no longer be assumed to be periodic. Perhaps more important, the breaking of waves should happen naturally in their propagation processes and should not be forced by the local body force. Therefore, a new model with nonperiodic vertical boundary condition and non-body forcing is needed as a first step to simulate the

breaking of internal gravity waves that propagate through the oceanic thermocline.

Here, the breaking of a monochromatic two-dimensional internal gravity wave is studied by using a newly developed spectral–pseudospectral model based on the "Channel Flow" code developed by Gibson et al. (2008). The model features vertical nonperiodic boundary conditions, which ensure a realistic simulation of wave breaking in the wave propagation. The internal wave breaking is studied with the emphasis on the distinctive roles of the convective instability and shear-induced instability, with each instability dominant in different regions of the wave field.

Our paper is organized as follows: Section 2 provides a detailed description of our model, especially in the setting of boundary conditions and the experimental design. Section 3 studies the evolution of isopycnal overturning and subsequent breaking of waves. Section 4 further studies the wave breaking in terms of the convective instability and shear-induced instability. Section 5 discusses the diapycnal mixing associated with the internal wave breaking and its relation to the real ocean. A summary and further discussion are given in section 6.

2. Model description

In this paper, a spectral–pseudospectral model has been applied to the ocean context for the first time. The computational domain of the model is an arbitrary layer in the main thermocline. A monochromatic two-dimensional internal gravity wave is forced from the top boundary and propagates down to the bottom. The background field is set at rest with a constant stratification and no mean shear flow. The model has nonperiodic boundary conditions in the vertical. It is important to point out that the internal gravity wave is excited by the top boundary condition instead of a body force.

a. Model formulation

We study an incompressible fluid whose dynamics are governed by the Navier–Stokes equations subject to the Boussinesq approximation in Cartesian coordinates. The x and y directions are horizontal, and z increases vertically upward. The total density consists of a constant reference part ρ_0 and a fluctuating part ρ. In the nonrotating frame, the governing equations of momentum and density are

$$\frac{\partial u_i}{\partial x_i} = 0, \tag{1}$$

$$\frac{\partial u_i}{\partial t} + u_j \frac{\partial u_i}{\partial x_j} = -\frac{\partial p}{\partial x_i} - g\frac{\rho}{\rho_0}\delta_{3i} + \nu\frac{\partial^2 u_i}{\partial x_j^2}, \quad \text{and} \tag{2}$$

$$\frac{\partial \rho}{\partial t} + u_j \frac{\partial \rho}{\partial x_j} = \kappa \frac{\partial^2 \rho}{\partial x_j^2}, \tag{3}$$

where p is the effective pressure that is equal to the ratio between the fluctuating part of the pressure and the reference density, ν is the kinematic viscosity coefficient, and κ is the diffusion coefficient of density. In Eqs. (1)–(3), the subscript $i = 1$, 2, and 3 denotes x, y, and z, respectively, and the Einstein summation convention is adopted.

In the case of a two-dimensional internal wave propagating though fluid with stable stratification, ρ can be further divided into two parts: the background profile $\overline{\rho}$ and the wave-induced perturbation ρ': that is, $\rho = \overline{\rho}(z) + \rho'(x, z, t)$. In the model, the background profile $\overline{\rho}$ is set as linear, with $d\overline{\rho}/dz < 0$ for the stable stratification. Then a background Brunt–Väisälä frequency N is deduced as $N^2 = -(g/\rho_0)(d\overline{\rho}/dz)$. The wave-induced density perturbation ρ' can be estimated form linear wave theory. By introducing a streamfunction $\Psi(x, z, t)$ such that $u = \psi_z, w = -\psi_x$, and the vorticity $\zeta = u_z - w_x = \nabla^2 \psi$; hence, equations for a linear wave can be written as

$$(\partial_t - \nu\nabla^2)\psi_z + p_x = 0, \tag{4}$$

$$(\partial_t - \nu\nabla^2)(-\psi_x) + p_z + \frac{\rho'}{\rho_0}g = 0, \quad \text{and} \tag{5}$$

$$(\partial_t - \kappa\nabla^2)\rho' + \frac{\rho_0}{g}N^2\psi_x = 0, \tag{6}$$

where $\nabla^2 = \partial_{xx} + \partial_{zz}$ is the two-dimension Laplace operator. For a progressive wave with wavenumber $\mathbf{k} = (k, m)$ and frequency ω, the dispersion relation is

$$\omega^2 + i(\nu + \kappa)(k^2 + m^2)\omega - \kappa\nu(k^2 + m^2)^2 - \frac{k^2N^2}{k^2 + m^2} = 0. \tag{7}$$

In our study, the wave forcing is prescribed at the top boundary with a real-valued frequency ω; thus, the vertical wavenumber m in Eq. (7) is a complex number that can be written as $m = m_r - im_i$, where the real part m_r denotes the vertical wavy structure and the imaginary part m_i denotes the vertical damping of wave amplitude. For the Prandtl number $P_r = \nu/\kappa = 1$, the group velocity is

$$\mathbf{C}_g = \frac{kmN^2\nu^2}{[A - i(B - \omega)]^2(B + iA)}(k, -m) - 2i\nu(k, m), \tag{8}$$

where $A = \nu(k^2 + m_r^2 - m_i^2)$ and $B = \omega + 2\nu m_r m_i$. In the paper, we denote C_{gx} and C_{gz} as the real parts

of the horizontal and vertical components of $\mathbf{C}_g$, respectively,

$$C_{gx} = \text{Re}\left\{\frac{km^2N^2\nu^2}{[A - i(B - \omega)]^2(B + iA)} - 2i\nu k\right\} \quad \text{and} \tag{9}$$

$$C_{gz} = \text{Re}\left\{\frac{-k^2mN^2\nu^2}{[A - i(B - \omega)]^2(B + iA)} - 2i\nu m\right\}. \tag{10}$$

The linear polarization relations can be written as

$$\psi(x, z, t) = \frac{a\omega}{k}\exp(m_i z)\cos(kx + m_r z - \omega t) \quad \text{and} \tag{11}$$

$$\rho'(x, z, t) = \frac{\rho_0 N^2 a\omega}{g(A^2 + B^2)}\exp(m_i z)[A\sin(kx + m_r z - \omega t) \\ + B\cos(kx + m_r z - \omega t)], \tag{12}$$

where a is the wave amplitude.

It should be noted that Eqs. (7)–(12) appear to imply that the wave parameters ω, k, m, A, B, etc., are all precisely known. This is true for the horizontal components of wavenumber, which are constrained by periodic lateral boundary conditions to be integral multiples of a basic unit. However, because the forcing amplitude a is a function of time in our experiments, the effective frequency and hence the vertical wavenumber are not precisely determined. However, the time scale over which a changes by a factor of 2 is long compared to ω^{-1}, which is the relevant scale for the internal wave dynamics. Thus, the results of the forcing resemble a wave packet rather than a strictly monochromatic wave. Though $(1/a)(da/dt)$ could easily be reduced, more computer time would be required and for studies of large-amplitude wave breaking the present values seem adequate.

In our study, a nondimensional form of wave amplitude is employed: the wave steepness $s = am_r$, which has a physical meaning as the ratio between the maximum wave-induced velocity u_{max} in x direction and the phase velocity c_x in the same direction: that is, $s = u_{max}/c_x$. It should be mentioned that Eqs. (4)–(12) are only used in setting the top boundary condition (details in section 2c). Flows in the computation domain are still governed by Eqs. (1)–(3).

b. Computational methods

The model is three dimensional with a computation domain of $2 \times 2 \times 4$ in the x, y, and z directions. A two-dimensional (x, z) wave is forced from the top boundary by employing a zero wavenumber in the y direction. The

horizontal wavelength is set be equal to domain length in the x direction (i.e., $L_x = 2$), and the horizontal wavenumber is $k = 2\pi/L_x = \pi$. The background Brunt–Väisälä frequency is set as $N = 0.7$. In the paper, associated variables such as vorticity will be shown with normalized by N; hence, our results are independent on the choice of the value of N. The forcing frequencies ω of waves are chosen between 0 and N, as $\omega \sim 0.143N$–$0.429N$. The vertical wavenumber m can be calculated from the dispersion relationship Eq. (7), and the vertical wavelength is $L_z = 2\pi/m_r$. The spatial resolution is (64, 4, 512) in the x, y, and z directions, which ensures a comparable resolution within one wavelength along the x and z directions. Because the flow is two dimensional in the x–z plane, in the y direction very coarse resolution is set to economize the computation time.

A pseudospectral solution algorithm is applied to Eqs. (1)–(3). By using the spectral collocation method described by Canuto et al. (1988), we employ a Fourier series representation of field variables in the horizontal (x, y) direction and a Chebyshev series representation of field variables in the vertical z direction. Then the velocity and density fields can be written into vector-valued Fourier × Fourier × Chebyshev expansions whose mathematical forms are

$$u = \sum_{k_x=-N_x/2+1}^{N_x/2} \sum_{k_y=-N_y/2+1}^{N_y/2} \sum_{n=0}^{N_z-1} \hat{u}_{k_x,k_y,n} T_n(z) e^{2\pi i(k_x x/L_x + k_y y/L_y)}, \tag{13}$$

$$w = \sum_{k_x=-N_x/2+1}^{N_x/2} \sum_{k_y=-N_y/2+1}^{N_y/2} \sum_{n=0}^{N_z-1} \hat{w}_{k_x,k_y,n} T_n(z) e^{2\pi i(k_x x/L_x + k_y y/L_y)}, \quad \text{and} \tag{14}$$

$$\rho = \sum_{k_x=-N_x/2+1}^{N_x/2} \sum_{k_y=-N_y/2+1}^{N_y/2} \sum_{n=0}^{N_z-1} \hat{\rho}_{k_x,k_y,n} T_n(z) e^{2\pi i(k_x x/L_x + k_y y/L_y)}, \tag{15}$$

where N_x, N_y, and N_z are the number of collocation points in x, y, and z directions; k_x and k_y are Fourier wavenumbers; $T_n(z) = \cos[n \arccos(z)]$ is the Chebyshev polynomial of order n; and $\hat{u}_{k_x,k_y,n}$, $\hat{w}_{k_x,k_y,n}$, and $\hat{\rho}_{k_x,k_y,n}$ are corresponding Chebyshev coefficients in the horizontal velocity, vertical velocity and density fields. After the Fourier–Chebyshev transform, the nonlinear terms (advection terms) are treated explicitly and calculated by collocation methods, with aliasing errors minimized with "2/3 rule" (Boyd 1989; Canuto et al. 1988, 2007). All other linear terms, including the terms of kinetic viscosity and density diffusion, are treated implicitly. To make our simulation as close as possible to the situation in the real ocean where the molecular viscosity and diffusion are extremely weak, we set $\nu = \kappa = 10^{-5}$, the smallest coefficients of kinematic viscosity and density diffusion for which the model remains stable. In the initial state, the fluid is at rest, with a linear, stable background stratification. Solutions are advanced in time using a third-order Runge–Kutta time stepping scheme (RK3) with variable time steps to minimize the computational cost of integration by maximizing the time step while keeping the Courant–Friedrichs–Lewy (CFL) number near a threshold of CFL = 0.9. The wave-induced mean flow is removed from the model in each advancing step so that the mean flow shear remains zero during the course of the simulation. The rationale for this removal is given in the discussion part of section 6.

c. Boundary conditions

The boundary conditions are horizontally periodic due to Fourier basis functions in x and y but nonperiodic in the vertical thanks to Chebyshev basis functions in z. A single two-dimensional wave is forced by the top boundary condition ($z = 0$) that will hereafter be referred as the surface forcing. From Eqs. (11) and (12), the surface forcing is set in the form of

$$\psi(x, z = 0, t) = \frac{a(t)\omega}{k} \cos(kx - \omega t + \phi_0) \quad \text{and} \tag{16}$$

$$\begin{aligned} \rho'(x, z = 0, t) = \frac{\rho_0 N^2 a(t)\omega}{g(A^2 + B^2)} [A \sin(kx - \omega t) \\ + B \cos(kx - \omega t) + \phi_0], \end{aligned} \tag{17}$$

where ϕ_0 is the initial phase at $z = 0$ and the wave amplitude $a(t)$ varies slowly with time. On one hand, by increasing the wave amplitude, we can generate isopycnal overturning with enhanced wave-induced density perturbations. On the other hand, as a result of isopycnal overturning and associated wave breaking during the wave propagation, linear wave theory cannot be used to

TABLE 1. Chart of experiment design. Three groups of experimental cases are set as group A (A1–A5), group B (B1–B5), and group C (C1–C7). Here, N is the Brunt–Väisälä frequency; ω is the forcing frequency of wave and $T = 2\pi/\omega$ is the wave period; m_r and m_i are the real and imaginary parts of m in Eq. (7), respectively; $s(t)$ is the nondimensional wave amplitude; ϕ_0 is the initial phase at $x = 0$ in Eqs. (16) and (17); and C_{gz} is the vertical group velocity as calculated from Eq. (10).

Case	ω	m_r	m_i	$s(t)$	ϕ_0	C_{gz}
A1	$0.429N$	6.62	0.01	$1.0 \times (t/4T)$	0	0.0370
A2	$0.357N$	8.22	0.03	$1.0 \times (t/4T)$	0	0.0265
A3	$0.286N$	10.54	0.07	$1.0 \times (t/4T)$	0	0.0174
A4	$0.214N$	14.31	0.21	$1.0 \times (t/4T)$	0	0.0100
A5	$0.143N$	21.62	1.05	$1.0 \times (t/4T)$	0	0.0046
B1	$0.286N$	10.54	0.07	$0.78 \times \tanh(t/0.25T)$	0	0.0174
B2	$0.286N$	10.54	0.07	$0.9 \times \tanh(t/0.25T)$	0	0.0174
B3	$0.286N$	10.54	0.07	$1.0 \times \tanh(t/0.25T)$	0	0.0174
B4	$0.286N$	10.54	0.07	$1.1 \times \tanh(t/0.25T)$	0	0.0174
B5	$0.286N$	10.54	0.07	$1.5 \times \tanh(t/0.25T)$	0	0.0174
C1	$0.286N$	10.54	0.07	$1.0 \times \tanh(t/0.25T)$	$\pi/4$	0.0174
C2	$0.286N$	10.54	0.07	$1.0 \times \tanh(t/0.25T)$	$\pi/2$	0.0174
C3	$0.286N$	10.54	0.07	$1.0 \times \tanh(t/0.25T)$	$3\pi/4$	0.0174
C4	$0.286N$	10.54	0.07	$1.0 \times \tanh(t/0.25T)$	π	0.0174
C5	$0.286N$	10.54	0.07	$1.0 \times \tanh(t/0.25T)$	$5\pi/4$	0.0174
C6	$0.286N$	10.54	0.07	$1.0 \times \tanh(t/0.25T)$	$3\pi/2$	0.0174
C7	$0.286N$	10.54	0.07	$1.0 \times \tanh(t/0.25T)$	$7\pi/4$	0.0174

predict the correct bottom boundary condition at the time when the wave reaches the bottom of the computation domain. Therefore, our model integration is terminated before any wave-induced perturbation moving at the approximate group velocity has gotten there. The velocity and density fields at the bottom boundary are set to zero during the integration.

As summarized in Table 1, three groups of cases have been designed for different purposes. The first group (A1–A5) aims to determine the critical steepness for isopycnal overturning in different waves; thus, the surface forcing is set to increase slowly and linearly with time. In this group, the nondimensional wave amplitude can be written as

$$s(t) = 1.0 \times \left(\frac{t}{4T}\right), \tag{18}$$

where $T = 2\pi/\omega$ is the wave period. As shown in Table 1, ω and m_r vary for different waves, but all the waves will reach a steepness of $s = 1$ at the end of the fourth wave period.

Based on the critical steepness from group A, the second group (B1–B5) features in flows induced by constant surface forcing that are equal to or beyond the critical steepness. In this group, we fix the forcing frequency of wave as $\omega = 0.286N$ and select various constants s_0 as the steady-state amplitude of the wave. Here, $s_0 = 0.78$ is the critical steepness determined from group A (A3) and

$s_0 = 1.0$ is the nominal threshold of convective instability; $s_0 = 0.9$ and $s_0 = 1.1$ constitute a comparison study for wave amplitudes both below and above nominal convective instability; and $s_0 = 1.5$ provides the case with strongest surface forcing. In applications, we also use a surface forcing in the following form

$$s(t) = s_0 \times \tanh\left(\frac{t}{0.25T}\right) \tag{19}$$

so that the wave amplitude increases from zero to the value s_0 within one wave period and remains constant afterward.

The third group (C1–C7), which is used for the study of diapycnal mixing, is the ensemble group of case B3. The estimation of diapycnal mixing needs averaging under steady forcing for a long time. For this purpose, the integrating period of B3 may be not long enough. Therefore, we designed seven ensemble cases C1–C7 for B3 and each of C1–C7 has the same setting with B3 but a different initial phase ϕ_0 in the surface forcing (Table 1).

3. Isopycnal overturning and wave breaking

Isopycnal overturning and associated convective instability arise in a progressive internal gravity wave as soon as the wave amplitude rises above a certain threshold, as shown in Fig. 1, which provides the depth–time diagram of the vorticity (normalized by N) and density fields at a sampling point of $x = -0.2L_x$. From Fig. 1, provided its amplitude is small, the primary wave is stable and propagating downward. This behavior is different from results of linear stability analysis that infinitesimally small-amplitude waves ($s \ll 1$) are unstable because of parametric subharmonic instability (PSI; Mied 1976; Drazin 1977; Klostermeyer 1982, 1991; Lombard and Riley 1996; Lombard 1996; Sonmor and Klaassen 1997). However, because the growth rate of PSI is smaller than the diffusive rate or the rate of other instabilities such as modulation instability (Sutherland 2006a), wave breaking occurs after the wave grows to sufficiently large amplitude. In our study, $\nu = \kappa = 10^{-5}$, so for disturbances with scales smaller than $1/10$ of the primary wavelength, the damping time scale is smaller than three wave periods. Thus, as shown in Fig. 1, viscosity and diffusivity effectively dampen the small disturbances before PSI has time to take effect. When the wave amplitude gets larger, anomalous flows accompanied by isopycnal overturning appear in the flow, parallel to certain phase lines. The wave propagation becomes contaminated but is not terminated by occurrences of anomalous flows and isopycnal overturning. As shown in Fig. 1b, the first isopycnal overturning happens at depth $z = -0.2L_z$ and at time
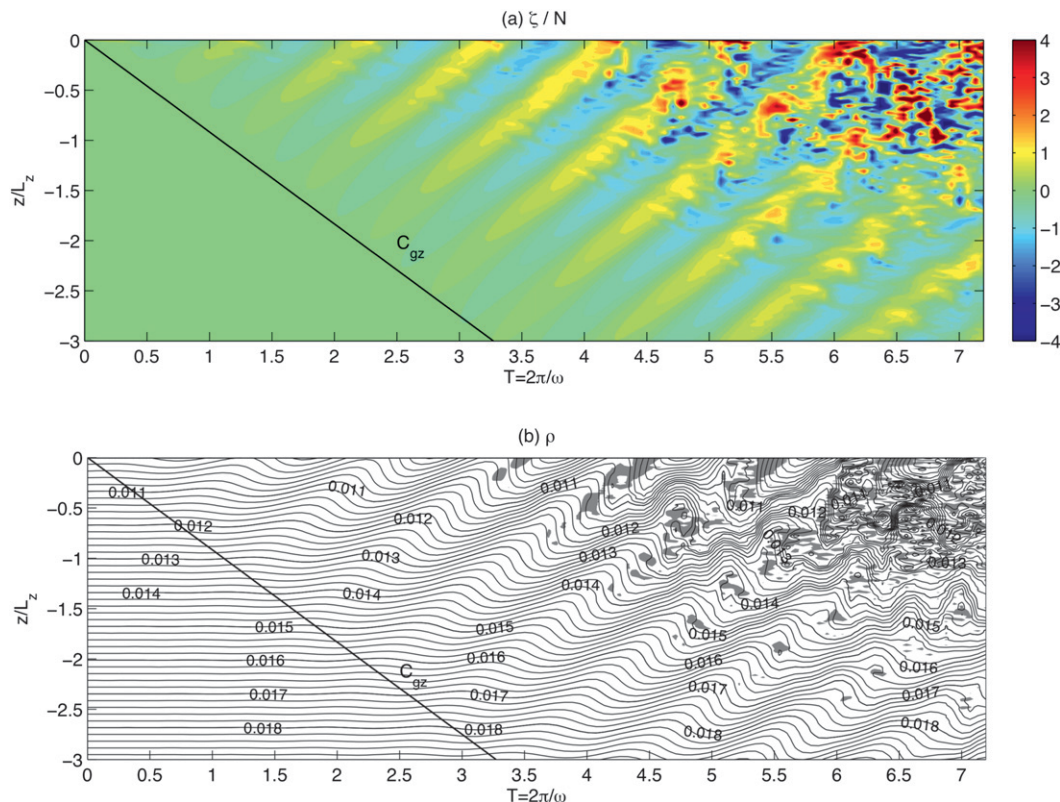
FIG. 1. Depth–time diagrams of (a) normalized vorticity ζ/N and (b) density ρ at the point $x = -0.2L_x$ in case A3 ($\omega = 0.286N$). Vorticity ζ in (a) is normalized by Brunt–Väisälä frequency N. In (b), isopycnal is contoured with interval of 2×10^{-4} and labeled with interval of 1×10^{-3}. Areas of $d\rho/dz \geq 0$ are shaded to indicate isopycnal overturning. In both plots, line (black solid) is plotted in each case with its slope equal to the vertical group velocity C_{gz} by Eq. (10).

$t = 3.3T$, which corresponds to the phase of the strongest velocities downward and to the right and also the largest wave-induced density perturbations to the background stratification (Fig. 2a). This first isopycnal overturning occurs before the time $t = 4T$ when the surface forcing reaches $s = 1$, and there are no anomalous flows happening in the period $t = 3.3T$–$4T$ (Figs. 2a,b). Anomalous flows appear and develop after $t = 4T$, such as a counterrotating vortex pair appearing at $t = 4.7T$ (Fig. 1a). The upper vortex centers at $x = -0.25L_x, z = -0.5L_z$ with anticlockwise rotation, and the lower vortex centers at $x = -0.2L_x, z = -1.1L_z$ with clockwise rotation (Fig. 2c). The vortex pair centers about the phase of the largest isopycnal distortions and results from the opposite wave-induced shears across the center phase. After continuous isopycnal overturning, the structure of counterrotating vortex pairs ceases to be distinguishable. The density field becomes finely structured and the flow becomes disordered (Fig. 2d), with corresponding continuous transfer of primary wave energy to smaller scales.

To examine isopycnal overturning in different waves, an overturning ratio is calculated in cases A1–A5 and shown in a depth–time (wave steepness) diagram (Fig. 3). The overturning ratio is defined as the ratio of the number of points having $d\rho/dz \geq 0$ (indicating isopycnal overturning) in the x–y plane on each z level to the total number of points within the x–y plane. As illustrated in Fig. 3, the critical steepness s_c is smaller than 1 in all the waves, which is likely due to the nonlinearity in the flows. Also, the critical steepness s_c varies little with different forcing frequencies. Specifically, $s_c = 0.75$ as $\omega = 0.429N$, $s_c = 0.78$ as $\omega = 0.214N$–$0.357N$, and $s_c = 0.79$ as $\omega = 0.143N$, indicating that isopycnal overturning occurs slightly later in a forcing wave with lower frequency. In addition, Fig. 3 shows a downward penetration of isopycnal overturning in the process of the wave propagation. However, as a result of damping by kinetic viscosity and density diffusion, the wave amplitude decreases vertically so that it no longer produces isopycnal overturning beyond a certain depth. As shown in Fig. 3, the penetration depth of isopycnal overturning relative to a vertical wavelength decreases with the forcing frequency. It extends over $z = 3L_z$ when $\omega = 0.429N$, extends over $z = 2.5L_z$ when $\omega = 0.286N$, and is least
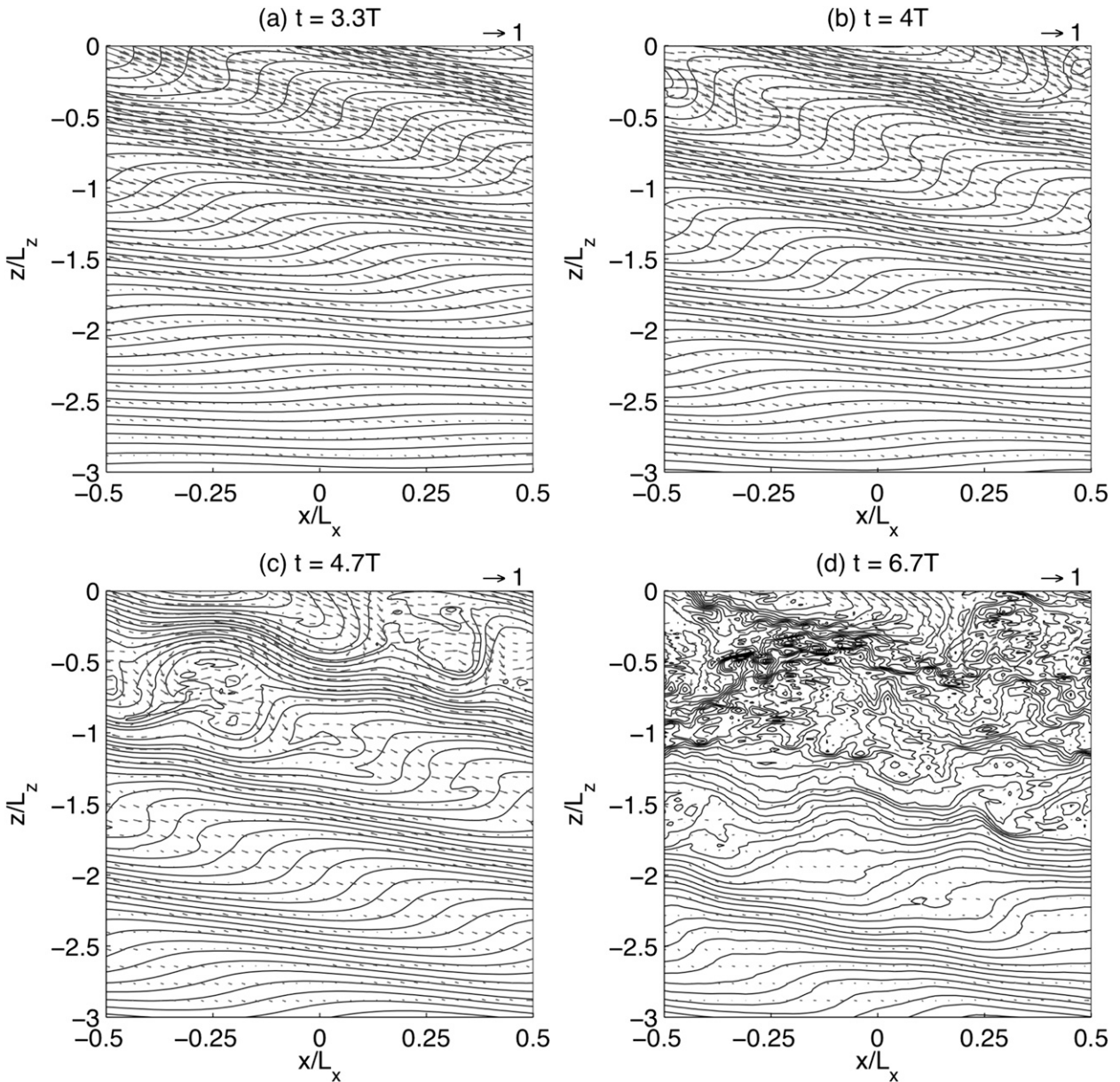
FIG. 2. Cross sections of the flows at (a) $t = 3.3T$, (b) $t = 4T$, (c) $t = 4.7T$, and (d) $t = 6.7T$ in case A3 ($\omega = 0.286N$). Isopycnal is contoured with interval of 1×10^{-3}. Velocities are plotted in vectors (u, w) in which u is normalized by the horizontal group velocity C_{gx} by Eq. (9) and w is normalized by the vertical group velocity C_{gz} by Eq. (10).

at $z = 0.5L_z$ as $\omega = 0.143N$. Such a dependence on ω may be inferred from Eq. (12) and Table 1, where the wave-induced density perturbation has a greater damping coefficient m_i for smaller ω. This reduces the chance in generating isopycnal overturning at deeper depths and finally leads to a shallower penetration depth.

As mentioned before, the development of anomalous flows indicates that the primary wave breaks into higher mode harmonics and transfers wave energy from the primary scale into smaller scales (Figs. 1, 2c,d). Now, we

will examine the energy transfer among different modes by examining the energy spectrum. The kinetic energy per unit volume are $E_u = u^2/2$ and $E_w = w^2/2$ for the horizontal and vertical velocity, respectively, and the potential energy is defined as $E_p = -(1/2)[g/(d\overline{\rho}/dz)]\rho'^2$ (Holliday and McIntyre 1981; Gill 1982). Also, we will focus on the integrated energy over the domain $[-2L_z, 0]$ in cases A1–A4, because most of isopycnal overturning and wave breaking happens in this range (Fig. 3). Figure 4 shows the normalized energy spectrum as the
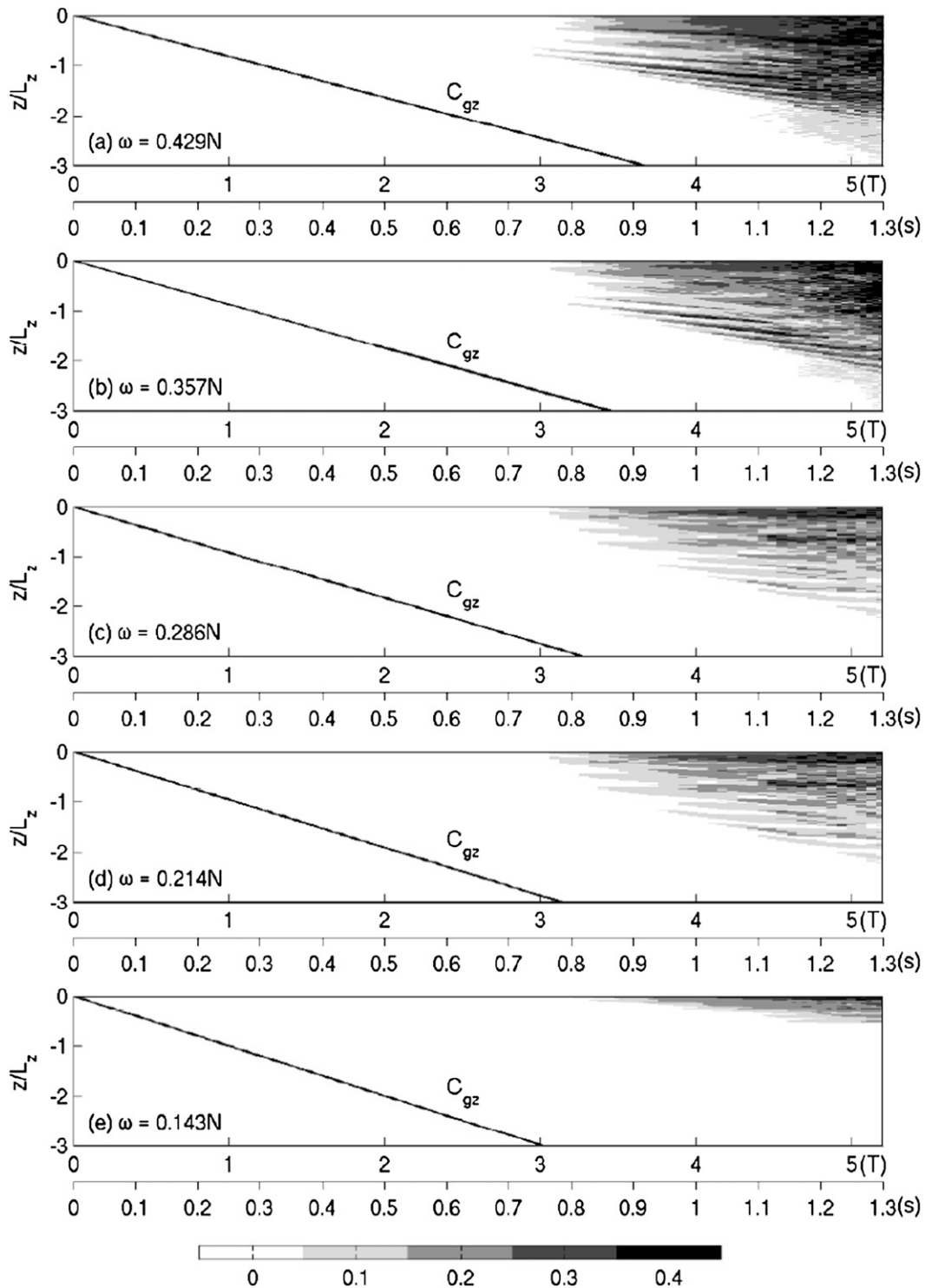
FIG. 3. Depth–time diagrams of overturning ratio in case (a) A1 ($\omega = 0.429N$), (b) A2 ($\omega = 0.357N$), (c) A3 ($\omega = 0.286N$), (d) A4 ($\omega = 0.214N$), and (e) A5 ($\omega = 0.143N$). Diagrams are also plotted against the surface forcing s, because s is set to be linear with time in group A. The overturning ratio is defined as the ratio between the number of points having $d\rho/dz \geq 0$ in each horizontal plane and the total number of points within the plane. Line (black solid) is plotted in each case with its slope equal to the vertical group velocity C_{gz} by Eq. (10).
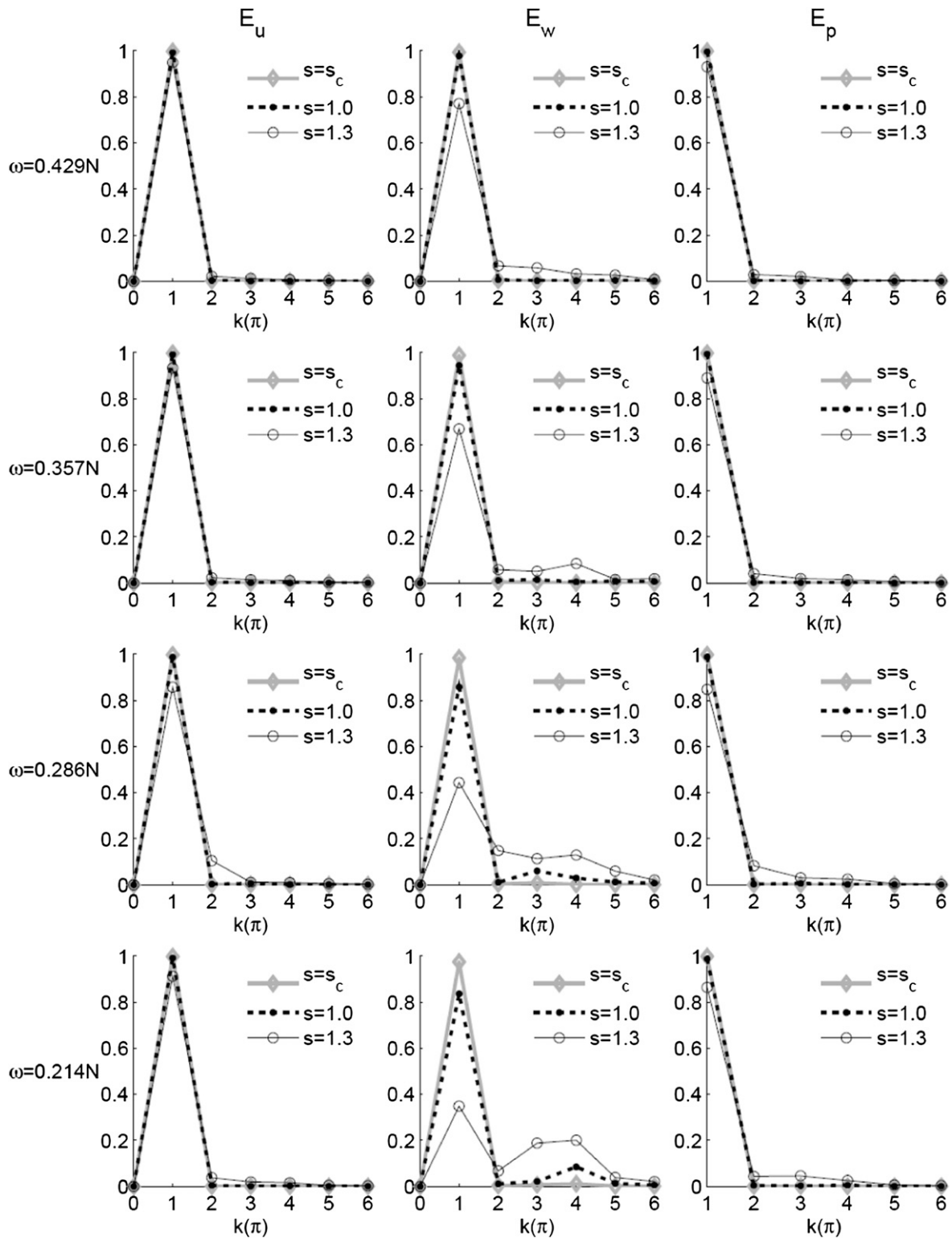
FIG. 4. Normalized energy spectrum as $s = s_c$, $s = 1$, and $s = 1.3$ in cases A1–A4. Shown are (left)–(right) the horizontal kinetic energy $E_u = u^2/2$, the vertical kinetic energy $E_w = w^2/2$, and the potential energy $E_p = -(\frac{1}{2})[g/(d\overline{\rho}/dz)]\rho'^2$. All energies are integrated over the domain $[-2L_z, 0]$. The critical steepness s_c equals 0.75 in case A1 and equals 0.78 in other cases.

surface forcing is equal to $s = s_c$, $s = 1$, and $s = 1.3$. In the initial isopycnal overturning ($s = s_c$), there is no generation of any high-order harmonic in the kinetic and potential energy spectrum. All the wave energy is concentrated on the primary scale $k = \pi$, which indicates that isopycnal overturning does not always imply simultaneous wave breaking but is a sufficient condition for subsequent wave breaking. As the surface forcing reaches $s = 1$, the energy spectrum changes little in the faster forcing waves ($\omega = 0.429N$ and $\omega = 0.357N$) but changes much more in the slower forcing waves ($\omega = 0.286N$ and $\omega = 0.214N$). The harmonic $k = 3\pi$ arises in the E_w spectrum of wave $\omega = 0.286N$ with 15% of the primary wave energy transferring to high-order harmonics. The harmonic $k = 4\pi$ arises in the E_w spectrum of wave $\omega = 0.214N$ at a cost of 18% primary wave energy transferred. When the surface forcing enhances to $s = 1.3$, more high-order harmonics become significant in the spectra of all the waves. High-mode harmonics appear more energetic in the E_w spectrum, which indicates that the wave energy is more inclined to transfer from the primary mode to the higher modes through the vertical velocity. Also, the energy transfer is more effective in the slower forcing wave. For example, 22% of the primary wave energy E_w is transferred in wave $\omega = 0.429N$, whereas 63% of the primary wave energy E_w is transferred in wave $\omega = 0.214N$.

As illustrated in both physical (Fig. 2) and spectral (Fig. 4) fields, high-mode harmonics do not arise immediately after occurrences of isopycnal overturning. This is confirmed by Fig. 5 in another respect, the evolution of high-mode harmonics $k = 2\pi$–6π in cases A1–A4. As shown in Fig. 5, most high-mode harmonics have rapid growth after the surface forcing reaches $s = 1$, which indicates that the nominal convective instability $s = 1$ acts as a precondition for the development of high-mode harmonics. Besides, harmonics of higher modes are more apt to develop in the slower forcing waves. In the wave of frequency $\omega = 0.429N$, harmonics $k = 2\pi$ and $k = 3\pi$ dominate the high-mode harmonics, with the harmonic $k = 4\pi$ being less significant. However, the harmonic $k = 4\pi$ becomes one of the dominant high-mode harmonics for wave $\omega = 0.214N$. Here, our calculations are two dimensional. However, Andreassen et al. (1998) has shown that the fully three-dimensional motions may be critical at the stage of initial convective instability.

4. Convective instability and wave-induced shear instability

Because an increasing surface forcing is employed in group A, the flow cannot reach a steady state during the integration period of the model. Therefore, a new group

of cases (group B) with constant surface forcing is designed for the study of steady wave-induced flows. Figure 6 displays the evolution of flows with constant surface forcing of various magnitudes. The left column shows the evolution of normalized vorticity fields at a sampling point $x = -0.2L_x$, and the right column shows the evolution of the overturning ratio in the domain. With the weakest surface forcing ($s = 0.78$) that just reaches the threshold of isopycnal overturning, only a few points of overturning appears in the flow, within a narrow phase range around the largest isopycnal distortions. As a result, the stratification is little changed from the initial, and the wave propagates at a speed following the vertical group velocity as estimated from the linear theory [Eq. (10)]. As the surface forcing becomes stronger ($s = 0.9$–1.5), isopycnal overturning happens in a much broader phase range. The overturning ratio increases with enhanced surface forcing so that the density field is greatly modified and becomes finely structured. Anomalous flows are produced as a result, with strong positive and negative vorticities to disturb the flow. The wave no longer propagates with the group velocity but at a faster speed. Similar characteristic of the increase in vertical advance is also posed in a study of modulationally unstable wave packet (Sutherland 2006b). It needs pointing out that most of isopycnal overturning is concentrated within three wavelengths from the surface in all cases B1–B5.

Then we selected case B3 as the control, together with another seven ensemble members (C1–C7), for a further study of instabilities in the flow under the surface forcing $s = 1$. Here, leaving the computational domain unaltered, we limit the study domain to $[-3L_z, 0]$ for two reasons: 1) most of isopycnal overturning happens in this domain (Fig. 6) and 2) a steady flow can be achieved after the wave has passed through this domain. As verified in Fig. 7, the integrated wave energy increases at first as deeper flows are induced by the progressing wave and then becomes steady after $t = 3.3T$ when the wave has propagated through the domain. It is interesting to note that the wave energy is initially the same among the ensemble members but turns out to be diverse after passage.

Now we study the instability in the steady wave-induced flow. On one hand, our previous results (Fig. 1) show that convective instability comes from isopycnal overturning and appears along the constant phase lines of large density perturbations, which is consistent with the analysis by Thorpe (1994). On the other hand, shear instability is also expected in our simulation, as a result of strong self-induced shears at the wave crests and troughs. Hence we, examine these two stabilities in our simulation, by means of a local Richardson number $R_i = -(g/\rho_0)(d\rho/dz)/\zeta^2$. Straightly speaking, for the density
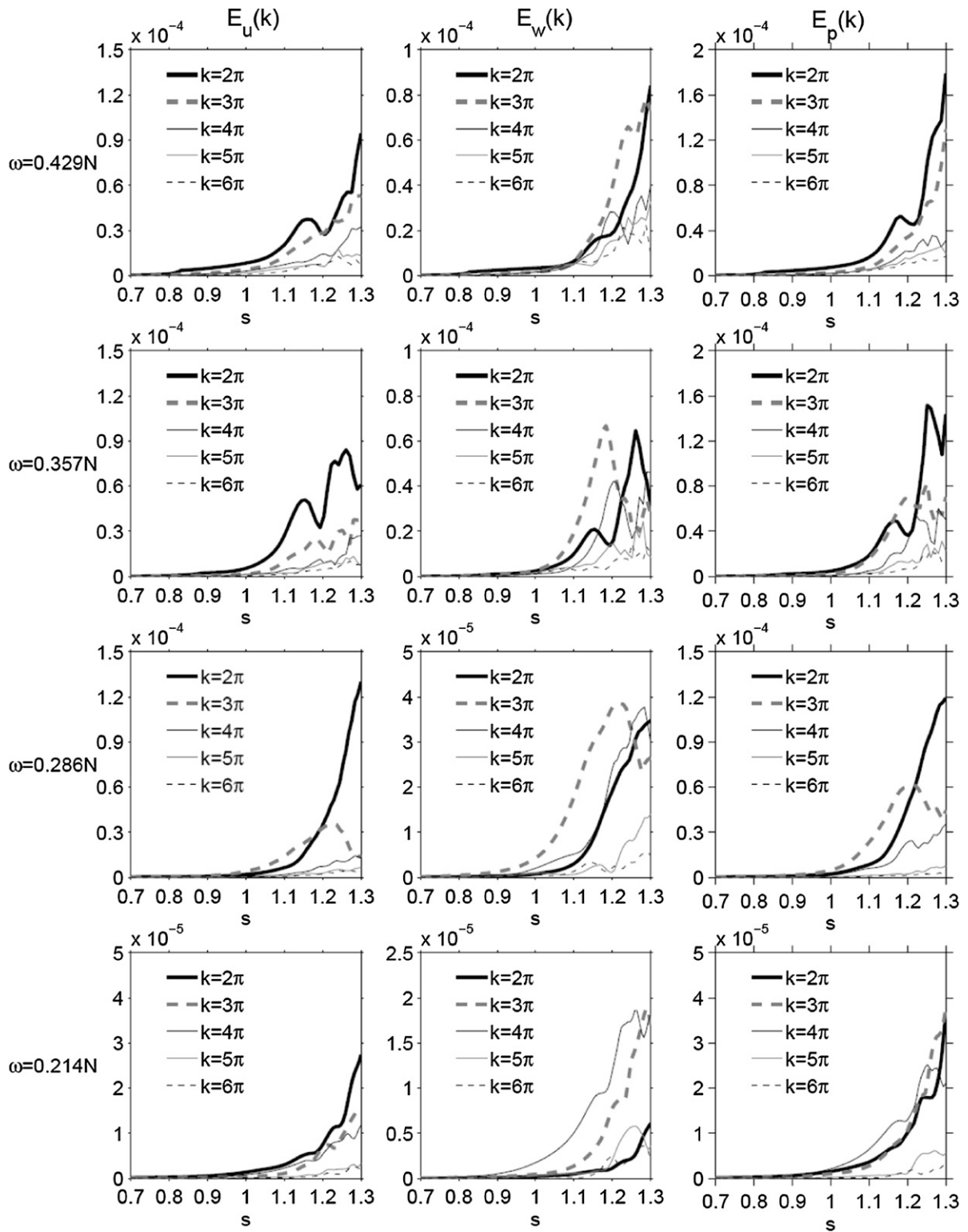
FIG. 5. Energy evolutions of high-mode harmonics $E_w = 2\pi$–6π in cases A1–A4. Shown are (left)–(right) kinetic energy E_u, E_w, and potential energy E_p of the high-mode harmonics integrated over the domain $[-2L_z, 0]$.
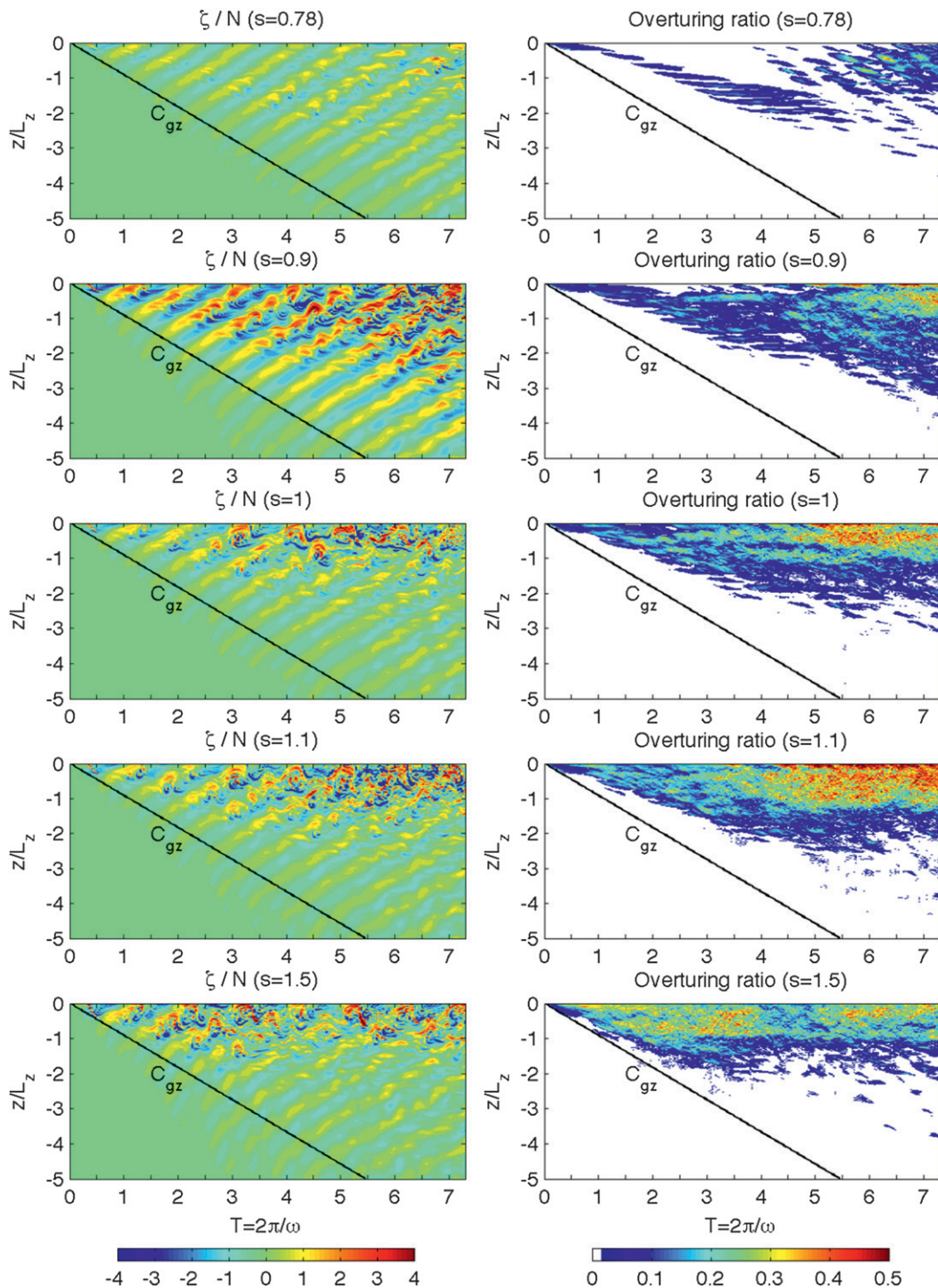
FIG. 6. (left) Depth–time diagrams of normalized vorticity ζ/N at the point $x = -0.2L_x$ in cases (top)–(bottom) B1–B5. (right) As in (left) but for overturning ratio in cases. Line (black solid) is plotted in each case with its slope equal to the vertical group velocity C_{gz} by Eq. (10).
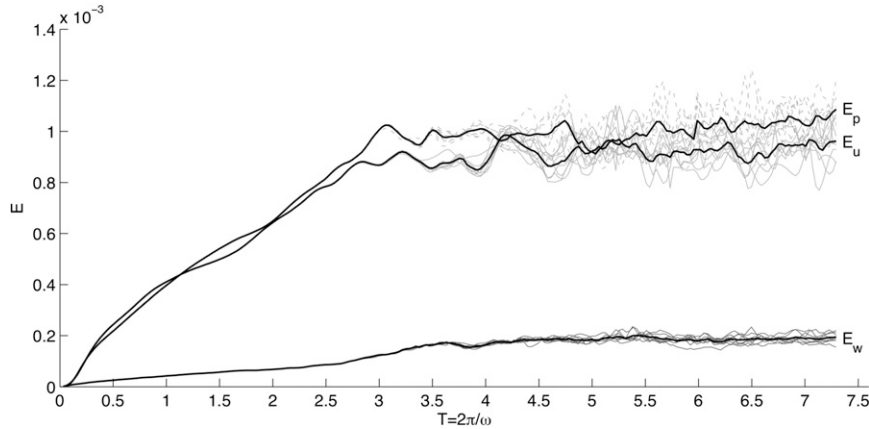
FIG. 7. Time series of volume-averaged energy for E_u (light gray, solid line), E_w (dark gray, solid line), and E_p (light gray, dotted line) over the domain $[-3L_z, 0]$ in eight ensemble cases (B3 and C1–C7). The ensemble mean is plotted in black.

gradient in the Richardson number definition, a derivative normal to the plane of the wave front would be more appropriate than the one used here in the vertical direction. However, for waves with moderately low frequencies as in our study, the differences between these two options in the density gradient are negligibly small.

Convective instability corresponds to $R_i \leq 0$, which comes from $d\rho/dz \geq 0$ as a local isopycnal overturning. Shear instability corresponds to $0 < R_i < 0.25$, which indicates strong self-induced shears overcoming the stable stratification. Figure 8 shows the convective instability and wave-induced shear instability in the steady flow at
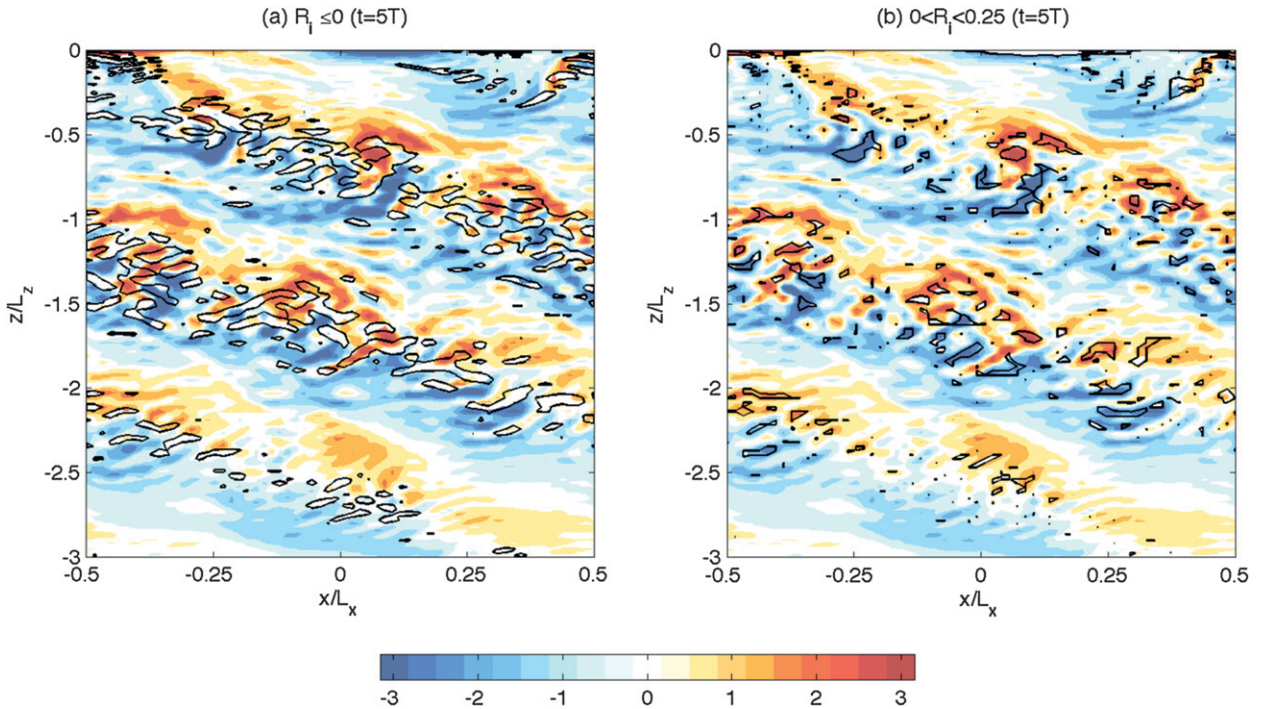
FIG. 8. Cross sections of normalized vorticity (colors) ζ/N and (a) $R_i \leq 0$ (contours) and (b) $0 < R_i < 0.25$ (contours) at $t = 5T$ in case B3. A local gradient Richardson number is defined as $R_i = -(g/\rho_0)(d\rho/dz)/\zeta^2$; $R_i \leq 0$ indicates convective instability and $0 < R_i < 0.25$ indicates wave-induced shear instability.
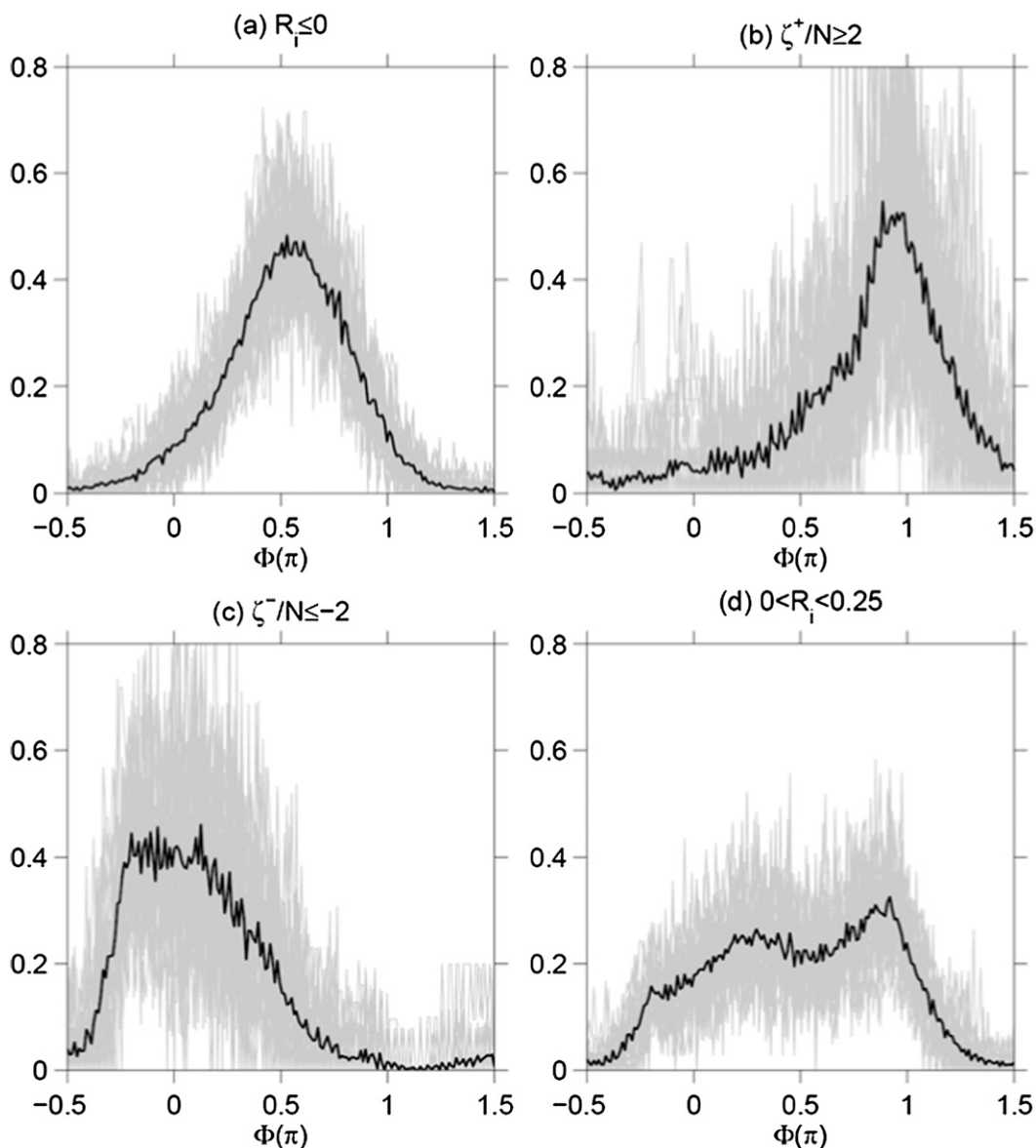
FIG. 9. PDF of (a) convective instability ($R_i \leq 0$), (b) with the strong positive self-induced shear indicated by the normalized vorticity $\zeta^+/N \geq 2$, (c) with the strong negative self-induced shear indicated by the normalized vorticity $\zeta^-/N \leq -2$, and (d) wave-induced shear instability ($0 < R_i < 0.25$) against wave phase in case B3. The referenced values of normalized vorticity $\zeta^\pm/N = \pm 2$ are used to represent strong self-induced shear and equal to shears at the wave crests and troughs under the background stratification in linear wave theory. PDFs (gray colored) are calculated from the flow fields $t = 4T$–$7T$ in case B3, with an interval of $0.25T$. The averaged PDFs are plotted in black.

time $t = 5T$. Convective instability occurs along the phase line between positive and negative vorticities where the wave-induced shears are weakest. Wave-induced shear instability is mostly generated at the wave crests and troughs, corresponding to billows with anomalous strong vortices.

From Fig. 8, convective instability and wave-induced shear instability have distinct characteristics in the phase distribution. These characteristics are further illustrated in Fig. 9, which displays probability density functions (PDFs) of both instabilities and strong self-induced shears ($|\zeta/N| \geq 2$) against the wave phase. In Fig. 9, 1) the self-induced shears are represented by the normalized vorticity ζ/N, and the referenced values of $\zeta^\pm/N = \pm 2$ correspond to the shears at the wave crests and troughs under the background stratification, as calculated from

linear wave theory, and 2) PDFs (gray colored) are calculated from the flow fields $t = 4T$–$7T$ in case B3, with an interval of $0.25T$. The averaged PDFs are shown in black. Obviously, PDFs of both instabilities in Fig. 9 have several characteristics consistent with linearly wave theory. For example, convective instability has a peak in probability at phase $\phi = \pi/2$ where the largest density perturbations are induced by the wave to undermine the background stratification (Fig. 9a). Wave-induced shear instability has a saddle pattern between $\phi = \pi$ and $\phi = 0$ (Fig. 9d), as a result of combined effects from reducing stratification toward $\phi = \pi/2$ (Fig. 9a) and increasing self-induced shears toward $\phi = \pi$ and $\phi = 0$ (Figs. 9b,c). However, nonlinearities in the flow make PDFs of both instabilities deviate from linear wave theory. As seen from Fig. 9a, PDF of convective instability drops smoothly from the center phase $\phi = \pi/2$ on both sides, covering most of the wave phases. However, the corresponding PDF from linear theory should appear as a delta function at $\phi = \pi/2$, because convective instability can only happen at the phase $\phi = \pi/2$ as $s = 1$. Also, in the simulation, wave-induced shear instability can still be generated in the phases dominated by convective instability (around $\phi = \pi/2$) but in a lower probability (Fig. 9d), which is impossible in linear theory because wave-induced shear is zero at $\phi = \pi/2$.

Figure 10 shows that PDFs of both instabilities have a characteristic transition from linearity to nonlinearity with increasing surface forcing. Convective instability ($s = 0.78$) has the PDF closest to the delta function at $s = 0.78$. With increasing surface forcing, convective instability has a flatter PDF peak at $\phi = \pi/2$ and a broader coverage of wave phases. As $s = 1.5$, convective instability can be generated in all wave phases. For wave-induced shear instability, it has the most distinct saddle shape of PDF between $\phi = \pi$ and $\phi = 0$ as $s = 0.78$, which is most consistent with the estimation from linear wave theory. This saddle-like distribution is undermined by the nonlinear effects as the surface forcing becomes stronger. Here, it merits attention that PDFs of both instabilities change little from $s = 0.9$ to $s = 1.0$ but alter much from $s = 1.0$ to $s = 1.1$, which is quite different from the result from linear stability analysis (Lombard and Riley 1996) that no major qualitative differences exist in instabilities between $s = 0.9$ and $s = 1.1$. This is consistent with the results shown in section 3 that most high-mode harmonics did not grow rapidly until the surface forcing goes beyond $s = 1.0$, which actually addressed the difference in instabilities between $s = 0.9$ and $s = 1.1$ here.

Finally, characteristics in the phase distribution of both instabilities are summarized in a concept diagram (Fig. 11). In linear wave theory, convective instability is confined within the overturning area and distinctly separated from wave-induced shear instability. Nonlinearities in the flow expand the phase range of both instabilities. As illustrated in Fig. 11, with nonlinearities included, there are some overlapping phases in PDFs of both instabilities, which indicated that both convective instability and wave-induced shear instability can occur in these phases.

5. Diapycnal mixing

The breaking of internal waves is accompanied by isopycnal distortions, leading to an irreversible diapycnal transfer of heat and salinity: that is, diapycnal mixing in the stably stratified fluid. Consistent with the estimation of diapycnal mixing in the oceanographic studies, we combine density fields for time $t = 4T$–$7T$ in eight ensemble cases (B3 and C1–C7) to enable stable averaging and then compute the average as the final stratification ρ_m for examining the diapycnal mixing. Figures 12a,b show a significant diapycnal mixing in the region $[-2.5L_z, 0]$, as indicated by a density flux of heavier water moving upward and lighter water moving down. Diapycnal mixing has a maximum modification of the initial stratification at $z = -0.5L_z$, corresponding to an enhanced vertical gradient of density flux there.

To quantify this mixing, an eddy diffusivity K_ρ is calculated from the vertical density flux $-\overline{\rho'w}$ and the mean vertical density gradient $d\rho_m/dz$ using the formula of $K_\rho = -\overline{\rho'w}/(d\rho_m/dz)$ (Osborn 1980; Winters and D'Asaro 1996; Barry et al. 2001). As shown in Fig. 12c, strong diapycnal mixing of $K_\rho \sim 1 \times 10^{-4}$ occurs beneath the surface and decays rapidly below $z = -0.5L_z$. This vertical decay of diapycnal mixing results from the kinetic viscosity and density diffusion in the model, which acts as a damping factor in the wave amplitude and undermines the wave breaking in the deeper depths.

We now examine the relationship between the strength of diapycnal mixing and surface forcing. As shown in Fig. 13, the K_ρ maximum increases from 1.5×10^{-5} as $s = 0.78$ to 2.15×10^{-4} as $s = 1.1$, which suggests that enhanced diapycnal mixing is generated in the flow induced by the stronger surface forcing. However, the strongest forcing ($s = 1.5$) does not lead to the strongest mixing, as the K_ρ maximum is 7.5×10^{-5}. This can be explained from Fig. 6 that considerable overturning occurred in the earlier stage $t = T$–$4T$ because of the forcing being so strong. As a result, some mixing is induced and the basic stratification is moderately modified. The modified stratification further inhibits the occurrence of overturning, finally resulting in a moderate mixing.

To compare our results with realistic oceanic flows, consider some nondimensional numbers such as the Froude number $F_r = m_r U/N$ and Reynolds number $R_e = UL/\nu$, where U denotes the root-mean-square magnitude
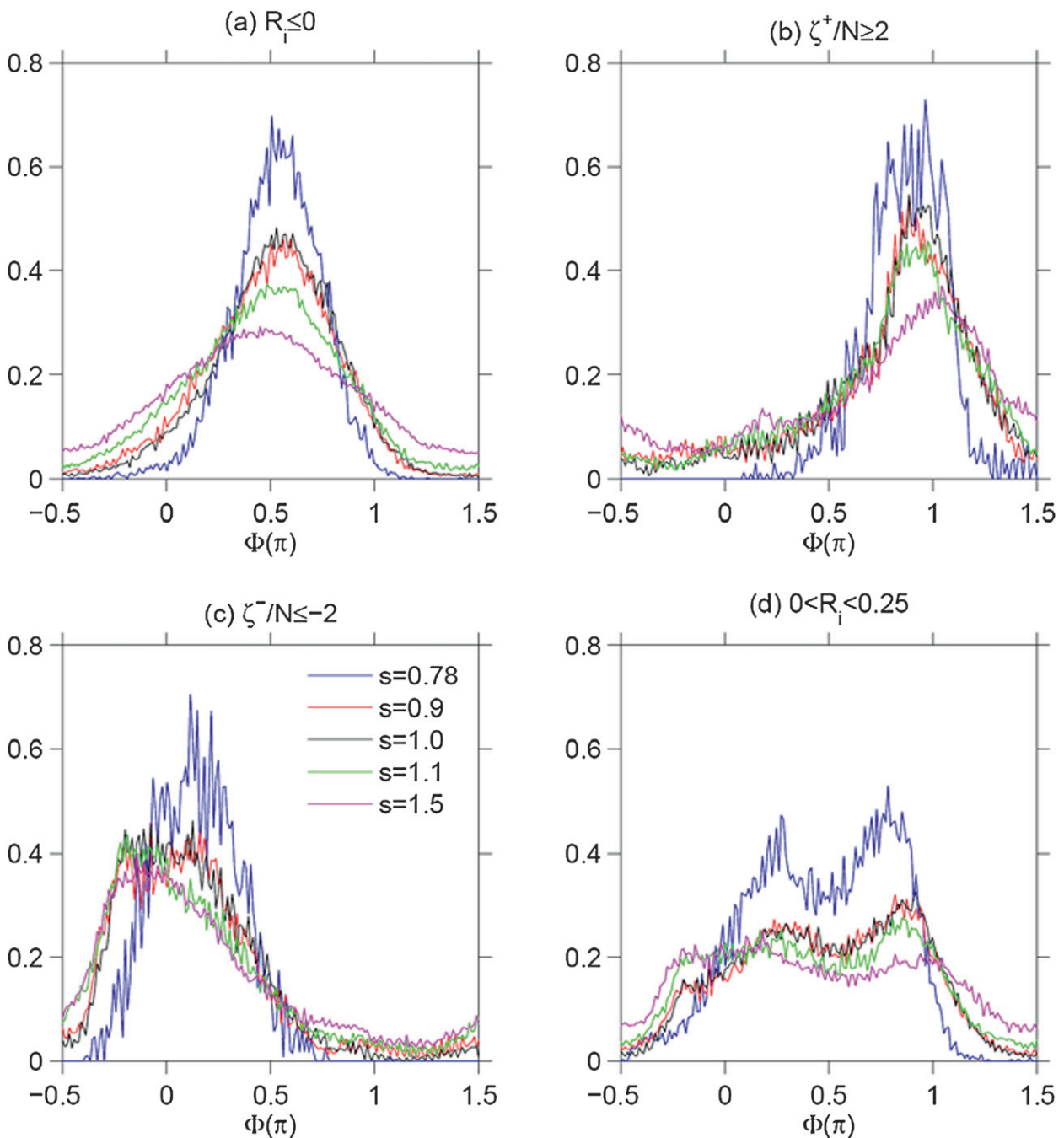
FIG. 10. As in Fig. 9, but for cases B1–B5. Only the averaged PDFs are plotted and colored in blue (B1), red (B2), black (B3), green (B4), and magenta (B5).

of the horizontal velocity. In our study, we take $L = L_x = 2$ and calculate U as the average horizontal velocity in the flow $t = 4T$–$7T$. As shown in Table 2, in our numerical simulations (B1–B5), the Froude numbers vary from 0.508 to 0.772, which is within the value range of the ocean ($F_r = 0.1$–1). On the other hand, the Reynolds

number in the numerical simulation is at least two orders smaller than that in the ocean. As shown in Table 3, $R_e \sim O(10^4)$ is currently the biggest Reynolds number our model can achieve, which is still far from the Reynolds number $R_e \sim O(10^7)$ in the real ocean. This may be because our simulation is restricted to two dimensions so that
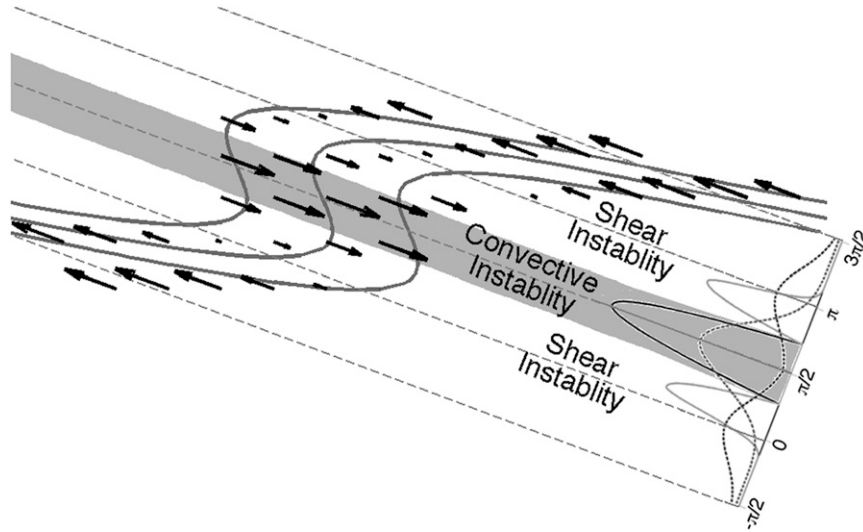
FIG. 11. Concept diagram of a large-amplitude wave ($s > 1$) with isopycnal (deep gray), velocity (black vectors), and overturning area (deep gray shaded). Two groups of PDFs are drawn; PDFs of convective instability and shear instability estimated from linear theory are plotted as solid lines and PDFs of convective instability and shear instability with nonlinearities included are plotted as dotted lines, and as summarized from cases B1–B5.

no isotropic turbulence develops and there is little energy transfer through the Kolmogorov cascade to smaller scales on which the molecular viscosity dominates dissipation.

In Table 2, diapycnal mixing is calculated in terms of the Cox number $\text{Cox} = K_\rho/\kappa$ (eddy diffusivity K_ρ normalized by molecular diffusivity κ) for comparison

with such diapycnal mixing in the ocean. As shown in Table 2, when the surface forcing just reaches the magnitude to generate isopycnal overturning ($s = 0.78$), wave breaking is little induced in the flow and diapycnal mixing of $\text{Cox} = 1.5$ is as weak as in a laminar regime. As the surface forcing reaches and exceeds $s = 1.0$, enhanced
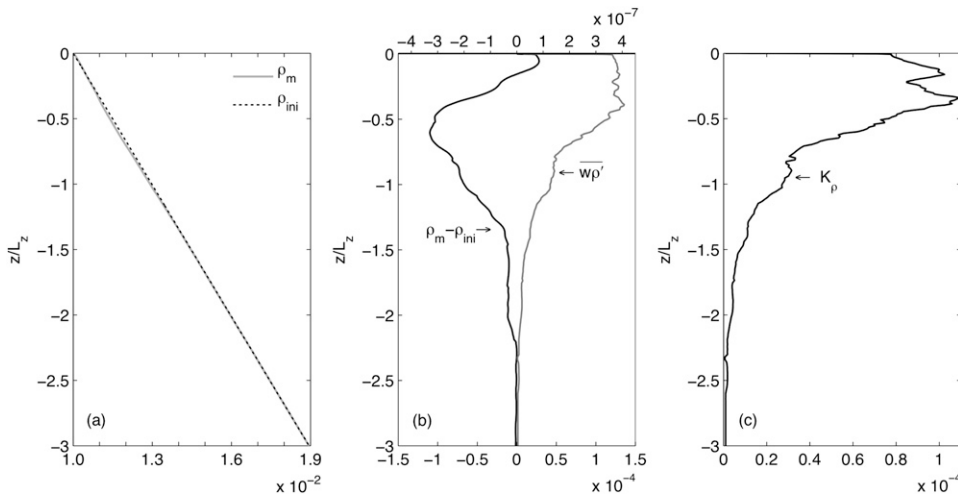
FIG. 12. (a) The final density profile ρ_m (gray solid) and initial density profile ρ_{ini} (black dotted); ρ_m is obtained by averaging the combined density fields $t = 4T–7T$ of eight ensemble cases (B3 and C1–C7). (b) Difference between ρ_m and ρ_{ini} (black) and the opposite of mean vertical density flux $-\overline{\rho'w}$ (gray); $-\overline{\rho'w}$ is calculated from the combined velocity and density fields $t = 4T–7T$ of eight ensemble cases (B3 and C1–C7). (c) The profile of turbulent diffusivity $K_\rho = -\overline{\rho'w}/(d\rho_m/dz)$ formulated as the ratio of the vertical density flux $-\overline{\rho'w}$ to the mean vertical density gradient $d\rho_m/dz$.
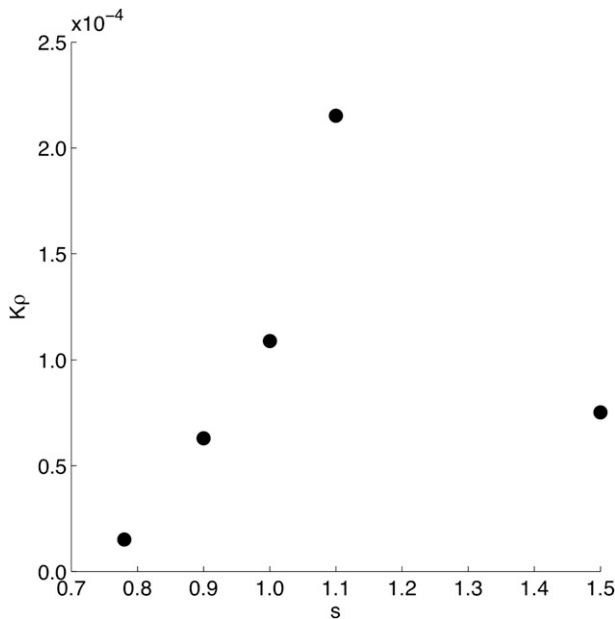
FIG. 13. Scatterplot of the turbulent diffusivity K_ρ maximum against the surface forcing. The K_ρ maximum corresponding to $s = 1$ is calculated from cases B3 and C1–C7. Other K_ρ maximums are calculated from cases B1, B2, B4, and B5.

wave breaking induces stronger mixing. When $s = 1.1$, the Cox number amounts to 21.5, which is in the lower range of reported values for the ocean Cox $\sim O(10^2)$ (Ivey et al. 2008).

Table 3 projects our nondimensional results (cases B1 and C1–C7) to their dimensional counterparts in the real ocean. For this purpose, we use representative oceanic values chosen to be consistent with the GM79 model developed by Garrett and Munk (1979) and Munk (1981). The Brunt–Väisälä frequency in the oceanic main thermocline is taken to be $N_O = 5 \times 10^{-3}$ s^{-1}.

Table 3 shows that our model can be treated as the simulation of the breaking of a primary wave with moderately low frequency of $\omega = 1.429 \times 10^{-3}$ s^{-1}, horizontal wavelength of 200 m, and vertical wavelength of 60 m. The wave frequency ω is selected to be $0.286N_O$ to match the available numerical simulations. The vertical wavelength of 60 m was chosen from those represented in GM79 as giving a 10-m vertical scale typical of wave-induced fine structure. Also from Table 3, the maximum horizontal velocity $u_{\max} = 0.05$ m s^{-1} is realistically achieved in the oceanic thermocline. That is to say, the condition $s \geq 1$ can be satisfied for the wave breaking. In addition, it should be pointed out that the primary wave with moderate frequency $\omega = 0.286N_O$ is not commonly matched to an obvious generation mechanism, but it can be generated by the superposition of many small-slope waves with different frequencies. From the mechanism

TABLE 2. Nondimensional number in flows under different constant forcing s: the Froude number F_r, the Reynolds number R_e, and the Cox number. Diapycnal mixing is shown by the Cox number, which is defined as eddy diffusivity K_ρ normalized by molecular diffusivity κ.

s	Cox	F_r	R_e
0.78	1.5	0.508	6.8×10^3
0.9	6.3	0.592	7.8×10^3
1.0	10.9	0.648	8.6×10^3
1.1	21.5	0.772	1.0×10^4
1.5	7.5	0.595	7.9×10^3

described in Bell (1978), a broad range of internal wave (with frequencies between the earth rotation f and N_O) could radiate from the base of mixed layer, and $\omega = 0.286N_O$ is in the middle of the range between f and N_O. On the lower end, the passing storms generate waves with low frequency close to f; on the upper end, Langmuir circulations can induce the high-frequency waves close to the buoyancy N_O (Polton et al. 2008). As a result of the superposition of waves with different frequencies, the primary waves $\omega = 0.286N_O$ can be obtained. Therefore, our results may shed some light on wave breaking in the real ocean.

6. Conclusions and discussion

This study sheds light on the breaking of large-amplitude progressive internal gravity waves. Using a newly developed spectral–pseudospectral model, a monochromatic two-dimensional primary wave of chosen frequency and horizontal wavenumber and with slowly increasing wave steepness is prescribed at the top boundary as forcing and propagates downward. For waves with forcing frequencies $\omega = 0.143N$–$0.429N$, the wave-induced density perturbations result in isopycnal overturning and associated convective instability when the steepness reaches

TABLE 3. Comparison between physical variables in the DNS of our study and those in the real ocean. In the DNS, variables are dimensionless and associated values are calculated from cases B3 and C1–C7. Values in the real ocean are consistent with GM79 model developed by Garrett and Munk (1979) and Munk (1981). The wave frequency is $\omega = 0.286N_O$, where $N_O = 5 \times 10^{-3}$ s^{-1} is the Brunt–Väisälä frequency adopted for the oceanic thermocline.

	DNS	Ocean
ω	0.2	1.429×10^{-3} s^{-1}
L_x	2.0	200 m
L_z	0.596	60 m
U	0.043	0.05 m s^{-1}
ν	1.0×10^{-5}	1.0×10^{-6} m^2 s^{-1}
R_e	8.6×10^3	1.0×10^7

the range $s_c = 0.75$–0.79. Isopycnal overturning is a sufficient condition for subsequent wave breaking, because when $s = s_c$ no primary wave energy is being transferred to high-mode harmonics, but high-mode harmonics grow rapidly beyond $s = 1$. In addition, lower-frequency primary waves showing a more efficient transfer of wave energy from the primary mode to higher modes.

A local gradient Richardson number is defined as $R_i = -(g/\rho_0)(d\rho/dz)/\zeta^2$ to separate convective instability ($R_i \leq 0$) from wave-induced shear instability ($0 < R_i < 0.25$). Consistent with linear theory, convective instability has a maximum in PDF at wave phase $\phi = \pi/2$ where the greatest density perturbations are induced by wave to counteract the background stratification, whereas shear instability has double maxima around $\phi = 0$ (wave trough) and $\phi = \pi$ (wave crest) saddled by a minimum at $\phi = \pi/2$. For both instabilities, however, the phase ranges are broadened significantly by nonlinearities introduced by the breaking waves.

Comparisons of our results with realistic oceanic flows are made through a similarity in the nondimensional numbers F_r and R_e. Diapycnal mixing is shown by the Cox number $\mathrm{Cox} = K_\rho/\kappa$, which is defined as eddy diffusivity K_ρ normalized by molecular diffusivity κ. The Cox numbers increase from 1.5 ($s = 0.78$) to 21.5 ($s = 1.1$), and the latter is in the low range of values in the ocean.

A monochromatic internal gravity wave whose amplitude can steepen over $s = 1$ probably never occurs in the ocean thermocline. There, internal gravity wave trains typically disperse until their steepness is small ($s \ll 1$) and wave breaking is more likely to be generated by a local superposition of multiple small-amplitude waves of comparable frequencies but different wavelengths, creating a patch of steepness s comparable to or greater than 1 that then evolves with its own, nonlinear dynamics. This situation may perhaps be simulated in our model by forcing from the top boundary with multiple, small-amplitude waves with random phase.

Also, no earth rotation f is included in present study. Actually, f is much smaller than the wave frequency ω in our study; thus, it is valid to neglect f. However, for the waves with very low frequency so that f is comparable to ω, rotation will introduce a velocity component transverse to the direction of wave propagation and associated transverse shear instability in convectively stable waves (Dunkerton 1984; Fritts and Rastogi 1985) and also will result in shear instability parallel to wave propagation by reducing the vertical wavelength (Dunkerton 1997). There is no preferred phase in the low-frequency waves at which the instability is mostly likely to occur (Lelong and Dunkerton 1998). Based on the conclusions from these previous researches, with rotation included, the PDF

of wave-induced instabilities in the current study would be totally changed and need examination in future work.

The present study of the mechanisms and signatures for the breaking of approximately monochromatic downward-propagating waves was intended as preparation for what would be a computationally much more demanding simulation of randomly superimposed waves, each individually of only moderate amplitude but collectively intermittently combining to exceed some threshold that triggers breaking and consequent turbulence. One potential issue in interpreting the present results is our treatment of the horizontal momentum associated with a downward-propagating wave. Theory requires that a linear internal gravity wave is associated with a horizontal momentum equal to its wave action times the horizontal component of its wavenumber (Bretherton 1969). Here, the wave action is the wave energy divided by the intrinsic frequency (i.e., its frequency relative to a frame of reference moving with the local average velocity of the fluid particles involved in the wave) and is a positive multiple of the wave amplitude squared, rather than of the wave amplitude itself. Because, unlike surface waves, internal gravity waves have no Stokes drift, when a wave packet propagates into a region that is otherwise at rest this wave momentum must be manifested as an $O(a^2)$ change in the average horizontal velocity within the volume occupied by the packet. In the vertical direction, the wave momentum is negated by the gravitational force associated with a vertical displacement of magnitude $O(a^2)$. However, for this study of downward-propagating progressive waves, the horizontal average velocity was maintained everywhere at zero.

The rationale for this decision was as follows: The best available dynamically consistent characterization of typical internal wave activity observed at many locations worldwide in the main thermocline is the GM79 model developed by Garrett and Munk (1979) and Munk (1981). This wave spectrum is everywhere horizontally isotropic, and at all wavenumbers the vertical wave energy fluxes are symmetric between upward and downward. These symmetries imply that at every location the net wave momentum and hence the wave-induced horizontally averaged velocities cancel out completely. Because the primary purpose of studying downward-propagating progressive waves of large amplitudes was to identify signatures of wave breaking and subsequent turbulence that might be useful in a numerical study simulating circumstances characteristic of the main thermocline, it seemed sensible to ignore such secondary effects of a coherent, large-amplitude, directional wave train.

Stimulated by the comments of an anonymous reviewer, a preliminary numerical experiment has revealed that retaining the horizontally averaged velocity associated with a downward-propagating progressive wave of significant amplitude can indeed make a large difference to the distributions of isopycnal overturning and fully developed turbulence. This difference appears to be related to the growth with time of a discrepancy in phase between the imposed forcing at the top boundary and that of the existing wave in the fluid below, and it may not be physically realistic. Further study will be necessary to resolve this issue.

REFERENCES

Andreassen, O., P. O. Hvidsten, D. C. Fritts, and S. Arendt, 1998: Vorticity dynamics in a breaking gravity wave, 1. Initial instability evolution. *J. Fluid Mech.,* **367,** 27–46.

Barry, M. E., G. N. Ivey, K. B. Winters, and J. Imberger, 2001: Measurements of diapycnal diffusivity in stratified fluids. *J. Fluid Mech.,* **442,** 267–291.

Bell, T. H., 1978: Radiation damping of inertial oscillations in the upper ocean. *J. Fluid Mech.,* **88,** 289–308.

Bouruet-Aubertot, P., C. Koudella, C. Staquet, and K. B. Winters, 2001: Particle dispersion and mixing induced by breaking internal gravity waves. *Dyn. Atmos. Oceans,* **33,** 95–134.

Boyd, J. P., 1989: *Chebyshev and Fourier Spectral Methods.* Springer, 792 pp.

Bretherton, F. P., 1969: On the mean motion induced by internal gravity waves. *J. Fluid Mech.,* **36,** 785–803.

Canuto, C., M. Y. Hussaini, A. Quarteroni, and T. A. Zang, 1988: *Spectral Methods in Fluid Dynamics.* Springer, 563 pp.

——, ——, ——, and ——, 2007: *Spectral Methods: Evolution to Complex Geometries and Applications to Fluid Dynamics.* Springer, 598 pp.

Drazin, P. G., 1977: On the instability of an internal gravity wave. *Proc. Roy. Soc. London,* **356A,** 411–432.

Dunkerton, T. J., 1984: Inertia–gravity waves in the stratosphere. *J. Atmos. Sci.,* **41,** 3396–3404.

——, 1997: Shear instability of internal inertia–gravity waves. *J. Atmos. Sci.,* **54,** 1628–1641.

Fritts, D. C., and P. K. Rastogi, 1985: Convective and dynamical instabilities due to gravity wave motions in the lower and middle atmosphere: Theory and observations. *Radio Sci.,* **20,** 1247–1277.

——, C. Bizon, J. A. Werne, and C. K. Meyer, 2003: Layering accompanying turbulence generation due to shear instability and gravity-wave breaking. *J. Geophys. Res.,* **108,** 8452, doi:10.1029/2002JD002406.

——, S. L. Vadas, K. Wan, and J. A. Werne, 2006: Mean and variable forcing of the middle atmosphere by gravity waves. *J. Atmos. Sol. Terr. Phys.,* **68,** 247–265.

——, L. Wang, J. Werne, T. Lund, and K. Wan, 2009a: Gravity wave instability dynamics at high Reynolds numbers. Part I: Wave field evolution at large amplitudes and high frequencies. *J. Atmos. Sci.,* **66,** 1126–1148.

——, ——, ——, ——, and ——, 2009b: Gravity wave instability dynamics at high Reynolds numbers. Part II: Turbulence evolution, structure, and anisotropy. *J. Atmos. Sci.,* **66,** 1149–1171.

Garrett, C., and W. Munk, 1979: Internal waves in the ocean. *Annu. Rev. Fluid Mech.,* **11,** 339–369.

Gibson, J. F., J. Halcrow, and P. Cvitanović, 2008: Visualizing the geometry of state space in plane Couette flow. *J. Fluid Mech.,* **611,** 107–130.

Gill, A. E., 1982: *Atmosphere–Ocean Dynamics.* Academic Press, 662 pp.

Gregg, M. G., 1987: Diapycnal mixing in the thermocline: A review. *J. Geophys. Res.,* **92** (C5), 5249–5286.

Holliday, D., and M. E. McIntyre, 1981: On potential energy density in an incompressible, stratified fluid. *J. Fluid Mech.,* **107,** 221–225.

Howard, L. N., 1961: Note on a paper of John W. Miles. *J. Fluid Mech.,* **10,** 509–512.

Ivey, G. N., K. B. Winters, and J. R. Koseff, 2008: Density stratification, turbulence, but how much mixing? *Annu. Rev. Fluid Mech.,* **40,** 169–184, doi:10.1146/annurev.fluid.39.050905.110314.

Klostermeyer, J., 1982: On parametric instabilities of finite-amplitude internal gravity waves. *J. Fluid Mech.,* **119,** 367–377.

——, 1991: Two and three-dimensional parametric instabilities in finite amplitude internal gravity waves. *Geophys. Astrophys. Fluid Dyn.,* **61,** 1–25.

Koudella, C. R., and C. Staquet, 2006: Instability mechanisms of a two dimensional progressive internal gravity wave. *J. Fluid Mech.,* **548,** 165–196.

Lelong, M. P., and T. J. Dunkerton, 1998: Inertia–gravity wave breaking in three dimensions. Part I: Convectively stable waves. *J. Atmos. Sci.,* **55,** 2473–2488.

Lombard, P. N., 1996: On the breakdown into turbulence of propagating internal waves. *Dyn. Atmos. Oceans,* **24,** 345–356.

——, and J. J. Riley, 1996: Instability and breakdown of internal gravity waves. I. Linear stability analysis. *Phys. Fluids,* **8,** 3271–3287.

McEwan, A. D., 1973: Interactions between internal gravity waves and their traumatic effect on a continuous stratification. *Bound.-Layer Meteor.,* **5,** 159–175.

Mied, R. P., 1976: The occurrence of parametric instability in finite amplitude internal gravity waves. *J. Fluid Mech.,* **78,** 768–786.

Miles, J. W., 1961: On the stability of heterogeneous shear flows: Part 2. *J. Fluid Mech.,* **16,** 209–227.

Munk, W., 1966: Abyssal recipes. *Deep-Sea Res.,* **13,** 707–730.

——, 1981: Internal waves and small scale processes. *Evolution of Physical Oceanography,* B. A. Warren and C. Wunsch., Eds., MIT Press, 264–291.

——, and C. Wunsch, 1998: Abyssal recipes II: Energetics of tidal and wind mixing. *Deep-Sea Res.,* **45,** 1977–2011.

Orlanski, I., and K. Bryan, 1969: Formation of the thermocline step structure by large-amplitude internal gravity waves. *J. Geophys. Res.,* **74,** 6975–6983.

Osborn, T. R., 1980: Estimates of the local rate of vertical diffusion from dissipation measurements. *J. Phys. Oceanogr.,* **10,** 83–89.

Polton, J. A., J. A. Smith, J. A. MacKinnon, and A. E. Tejada-Martinez, 2008: Rapid generation of high-frequency internal waves beneath a wind and wave forced oceanic surface mixed layer. *Geophys. Res. Lett.,* **35,** L13602, doi:10.1029/2008GL033856.

Polzin, K., R. W. Schmitt, J. M. Toole, and J. R. Ledwell, 1997: Spatial variability of turbulent mixing in the deep ocean. *Science,* **276,** 93–96.

Sonmor, L. J., and G. P. Klaassen, 1997: Toward a unified theory of gravity wave stability. *J. Atmos. Res.,* **54,** 2655–2680.

Stommel, H., and J. Webster, 1962: Some properties of thermocline equations in a subtropical gyre. *J. Mar. Res.,* **20,** 42–56.

Sutherland, B. R., 2001: Finite-amplitude internal wavepacket dispersion and breaking. *J. Fluid Mech.,* **429,** 343–380.

——, 2006a: Wave instability: Wave-wave versus wave-induced mean flow interactions. *Phys. Fluids,* **18,** 074107, doi:10.1063/1.2219102.

——, 2006b: Weakly nonlinear internal gravity wavepackets. *J. Fluid Mech.,* **569,** 249–258.

Thorpe, S. A., 1978: On internal gravity waves in an accelerating shear flow. *J. Fluid Mech.,* **88,** 623–639.

——, 1979: Breaking internal waves in shear flows. *Proc. 12th Symp. on Naval Hydrodynamics,* Washington, DC, National Academy of Science, 623–628.

——, 1994: Statically unstable layers produced by overturning internal gravity waves. *J. Fluid Mech.,* **260,** 333–350.

Winters, K. B., and E. A. D'Asaro, 1996: Diascalar flux and the rate of fluid mixing. *J. Fluid Mech.,* **317,** 179–193.